A novel MRI-based data fusion methodology for efficient, personalised, compliant simulations of aortic haemodynamics*

Catriona Stokes[a,1], Mirko Bonfanti[a,2], Zeyan Li[b,3], Jiang Xiong[c,4], Duanduan Chen[b,5], Stavroula Balabani[a,6], Vanessa Díaz-Zuccarini[a,7]

[a] *Mechanical Engineering Department, University College London, Torrington Place, London, WC1E 7JE, United Kingdom*
[b] *School of Life Science, Beijing Institute of Technology, Beijing, 100081, China*
[c] *Department of Vascular and Endovascular Surgery, Chinese PLA General Hospital, Beijing, 100083, China*

---

[*] **Word Count (Introduction through Discussion): 3481**

[1] catriona.stokes.18@ucl.ac.uk, ORCID:0000-0002-9112-9568
[2] m.bonfanti@ucl.ac.uk, ORCID: 0000-0001-5548-3298
[3] 3120181382@bit.edu.cn
[4] xiongjiangdoc@126.com, ORCID: 0000-0002-9884-1267
[5] duanduan@bit.edu.cn
[6] s.balabani@ucl.ac.uk, ORCID: 0000-0002-6287-1106
[7] v.diaz@ucl.ac.uk, ORCID: 0000-0003-3183-7463

Preprint submitted to Journal of Biomechanics *May 6, 2021*

Abstract

We present a novel, cost-efficient methodology to simulate aortic haemodynamics in a patient-specific, compliant aorta using an MRI data fusion process. Based on a previously-developed Moving Boundary Method, this technique circumvents the high computational cost and numerous structural modelling assumptions required by traditional Fluid-Structure Interaction techniques. Without the need for Computed Tomography (CT) data, the MRI images required to construct the simulation can be obtained during a single imaging session. Black Blood MR Angiography and 2D Cine-MRI data were used to reconstruct the luminal geometry and calibrate wall movement specifically to each region of the aorta. 4D-Flow MRI and non-invasive pressure measurements informed patient-specific inlet and outlet boundary conditions. Simulated wall movement closely matched 2D Cine-MRI measurements throughout the aorta, and physiological pressure and flow distributions in CFD were achieved within 3.3% of patient-specific targets. Excellent agreement with 4D-Flow MRI velocity data was observed. Conversely, a rigid-wall simulation under-predicted peak flow rate and systolic maximum velocities whilst predicting a mean Time-Averaged Wall Shear Stress (TAWSS) 13% higher than the compliant simulation. The excellent agreement observed between compliant simulation results and MRI is testament to the accuracy and efficiency of this MRI-based technique.

Keywords: Aorta, Computational Fluid Dynamics (CFD), Fluid Structure Interaction, Patient-specific simulation, Haemodynamics

---

1. Introduction

Computational Fluid Dynamics (CFD) and phase-contrast Magnetic Resonance Imaging (PC-MRI) techniques such as Four-Dimensional Flow MRI (4D-Flow MRI) are used to analyse arterial haemodynamics, providing valuable insights to support clinical decision-making. Due to limitations in spatio-temporal resolution, 4D-Flow MRI cannot accurately capture small-scale flow features such as the fluid boundary layer, and hence cannot accurately estimate clinically-relevant indices such as Wall Shear Stress (WSS) that are implicated in the onset and development of various cardiovascular diseases (Castagna et al., 2021; Mazzi et al., 2020; Miyazaki et al., 2017; Piatti et al., 2017; Zimmermann et al., 2018). Informing CFD simulations with medical imaging data can facilitate both high resolution and patient-specific accuracy, yielding higher-quality haemodynamic data than any individual modality could provide. However, simulation accuracy depends on the choice of modelling assumptions such as vessel wall compliance.

Modelling wall compliance is fraught with difficulties, so a rigid-wall assumption is commonly used. Unfortunately, this assumption has been shown to significantly affect the accuracy of haemodynamic metrics such as WSS (Lantz et al., 2011; Miyazaki et al., 2017; Qiao et al., 2019). Fluid-Structure Interaction (FSI), a technique that couples the structural dynamics of the vessel wall with the flow solution, is traditionally used to simulate compliance. However, the complex, inhomogeneous material properties of the aortic wall cannot be directly measured *in-vivo*. Instead, a uniform literature value of Young's Modulus (E) is often assumed (He et al., 2021; Ryzhakov et al., 2019; Saitta et al., 2019; Tang et al., 2020). This assumption fails to accurately capture vessel wall movement throughout the aorta, even when a range of E values are assessed.

A Moving Boundary Method (MBM) was developed by Bonfanti et al. (2017) to circumvent the structural assumptions and computational cost associated with FSI. Using CT data to reconstruct the aortic lumen and 2D Cine-MRI data to compute vessel wall compliance locally in each region of the aorta, the MBM can accurately capture wall movement throughout the aorta, unlike FSI. MBM simulations of Type-B Aortic Dissection (TBAD), a severe pathology characterised by a tear in the innermost layer of the aortic wall, agreed closely with an equivalent FSI simulation yet required only half the simulation time (Bonfanti et al., 2018). However, CT images are not always available, for example in healthy patients where the exposure to high doses of ionising radiation are not clinically justified. MRI-based techniques have therefore been developed, but typically employ a rigid-wall assumption (Bozzi et al., 2017; Madhavan and Kemmerling, 2018; Youssefi et al., 2017).

Several MRI-based FSI studies of healthy aortae have appeared in the literature, including those of Lantz et al. (2011), Boccadifuoco et al. (2018) and Pons et al. (2020). Each used a uniform value of E throughout the aorta, requiring multiple FSI simulations for its calibration. Lantz et al. (2011) and Boccadifuoco et al. (2018) used several literature values of E in the physiological range, whereas Pons et al. (2020) iteratively adjusted E by calibrating the pulse wave velocity (PWV) using estimations from 4D-Flow MRI. Comparisons against MRI data found that FSI failed to accurately capture wall movement throughout the aorta when uniform E was observed. Thus, there remains a need for cost-efficient, MRI-based CFD methods to accurately characterise non-uniform arterial compliance.

This study presents a novel MBM-based methodology to construct patient-specific, compliant simulations of a healthy thoracic aorta using a unique MRI data fusion process. MRA with 2D Cine-MRI is used to segment the aorta and calibrate region-specific wall movement, while 4D-Flow MRI with non-invasive pressure measurements informs patient-specific boundary conditions. Compared with FSI, the proposed CFD methodology can provide accurate results in significantly less time, using data from a single MRI acquisition session. This technique could facilitate shorter clinical decision-making timescales and reduce clinical resource requirements.

2. Methods

2.1. Clinical Data

Three MRI sequences of the thoracic aorta of a healthy volunteer were acquired using a Philips Achieva 3.0 TX multi-source MRI scanner at Beijing Institute of Technology, Beijing, China (Philips Medical Systems, Holland). MRA images of the thoracic aorta at diastole were acquired with a resolution of 0.48 x 0.48 x 1 mm^3. 2D Cine-MRI images were acquired as transverse planes with a resolution of 1.25 x 1.25 x 4 mm^3 and a timestep of 38 ms. Finally, sagittal 4D-Flow MRI images were acquired at 24 points across the cardiac cycle with a voxel size of 2.5 x 2.5 x 2.8 mm^3 and a single velocity encoding (VENC) of 1 m/s. A heart rate of 68 beats per minute and systolic and diastolic brachial blood pressures (P_{sb}, P_{db}) of 117 mmHg and 72 mmHg were measured using a sphygmomanometer after MRI acquisition. This work was ethically approved by the Institutional Review Board of the Chinese PLA

General Hospital (S201703601).

2.2. Geometry and Meshing

[Figure 1 about here.]

The simulation workflow is shown schematically in Figure 1. A patient-specific luminal geometry was reconstructed by manual segmentation of MRA data using Mimics (Materialize NV, Leuven, Belgium) (Figure 1a). The segmentation was bounded by an inlet at the ascending aorta (AA) and an outlet at the abdominal aorta (AbAo). Proximal sections of the supra-aortic branches, the Brachiocephalic Trunk (BT), Left Common Carotid (LCC), and Left Subclavian Artery (LSA), were included. MRA could not resolve the small arteries that branch from the descending thoracic aorta, so they were omitted. The cross-sectional area of the segmented aortic arch and proximal descending aorta was approximately 30% smaller than the equivalent 2D Cine-MRI areas. This is likely due to separation-induced flow stagnation in this region, which can reduce image contrast and erroneously indicate the presence of wall tissue (Henningsson et al., 2020). Fusing MRA and 2D Cine-MRI, selected regions of the segmented aorta were dilated by up to 2 mm in the surface-normal direction using Simpleware ScanIP (Synopsis Inc., CA, USA) to match the cross-sectional area measurements from 2D Cine-MRI whilst preserving the morphology of the lumen. The segmented geometry was used to construct a tetrahedral computational mesh with 525k elements using Ansys Fluent 20.0 (Ansys Inc., PA, USA) (Figure 1b). Details on prismatic layer settings are provided in Appendix A. Mesh refinement was determined using a mesh independence study described in Appendix B.

2.3. Boundary Conditions

The choice of inlet and outlet boundary conditions are critical to reproduce patient-specific physiological flow and pressure distributions. The inlet flow rate waveform was extracted from 4D-Flow MRI data at the ascending aorta using GTFlow (GyroTools LLC., Zurich, Switzerland). Using spline interpolation in MATLAB (MathWorks Inc., Natick, Massachusetts, USA), a smooth waveform with 1 ms increments, $Q_{SI}(t)$, was derived from these measurements and used to compute a uniform velocity inlet profile $v_{inlet}(t) = Q_{SI}(t)/A_{inlet}$ (Figure 1c). The application of a measured velocity inlet profile has been shown to produce equivalent results beyond two diameters of the inlet to uniform inlet profiles with the same inlet flow rate (Armour et al., 2020; Goubergrits et al., 2013; Madhavan and Kemmerling, 2018; McElroy and Keshmiri, 2018; Pirola et al., 2018).

Three-element Windkessel (WK3) outlet pressure boundary conditions were applied at each CFD outlet to simulate the effects of the peripheral vascular system and minimise the incidence of non-physical pressure wave reflections (shown schematically in Figure 1). Patient-specific WK3 calibration requires target values of inlet systolic and diastolic pressure (P_{sa}, P_{da}) and mean outlet flow rates. Diastolic pressure remains relatively constant throughout the arterial tree whilst systolic pressure increases, so P_{da} was set equal to P_{db} and P_{sa} was derived from the brachial systolic pressure P_{sb} using $P_{sa} \approx 0.83 P_{sb} + 0.15 P_{db}$ (Westerhof et al., 2010). The target mean flow rate at each outlet was then derived from 4D-Flow MRI data. As one voxel accounted for 10-30% of the cross-sectional area of each branch, measurements of supra-aortic branch flow rates from 4D-Flow MRI incurred high uncertainties. Instead, flow rate waveforms were first extracted at four planes in the descending aorta (DA1 - DA4 in Fig. 1). The total mean flow rate through the supra-aortic branches, $\bar{Q}_{SA}$, was then calculated as

$$\bar{Q}_{SA} = \bar{Q}_{inlet} - \frac{\bar{Q}_{DA1} + \bar{Q}_{DA2} + \bar{Q}_{DA3} + \bar{Q}_{DA4}}{4} \tag{1}$$

and $\bar{Q}_{SA}$ was split proportionally between each branch based on their respective diastolic cross-sectional area.

Each WK3 is an electrical analogue consisting of a proximal resistance (R_p^i), a distal resistance (R_d^i) and a capacitance (C_{WK3}^i) whose values must be carefully calibrated. A 0D lumped parameter model of the aorta was used to tune the WK3 parameters (Figure 1e). The CFD domain was represented by a number of discrete segments (RLC units), each containing a resistor (R^i), an inductor (L^i) and a capacitor (C_V^i) to simulate fluid pressure loss, inertance and volume compliance due to wall movement, respectively. A WK3 was connected to each outlet of this 0D model, and the inlet flow rate waveform $Q_{SI}(t)$ was applied at the inlet. The resulting system of ordinary differential equations was solved numerically using 20-sim (ControllabProducts B.V., Enschede, The Netherlands) by backward differentiation. For each RLC unit, R^i were computed using the total pressure loss through each segment from a steady-state CFD simulation at the mean inlet flow rate. L^i were calculated using an expression for large arteries of length l^i and cross-sectional area A^i:

$$L^i = (4/3)\rho l^i \cdot {A^i}^{-1} \tag{2}$$

where ρ is the density of blood (Westerhof et al., 2010). The volume compliances C_V^i were calculated as

$$C_V^i = D^i \cdot V^i \tag{3}$$

where V^i is the volume of the segment. D^i is the local wall distensibility which is calculated from 2D Cine-MRI measurements of cross-sectional area at each segment as

$$D^i = \frac{\Delta A^i}{A^i_{min}} \cdot \frac{1}{P_{pulse}} \tag{4}$$

where ΔA^i is the maximum cross-sectional area change across the cardiac cycle and A^i_{min} is the diastolic area. Because the supra-aortic branches were not resolved by 2D Cine-MRI, their respective distensibilities were calculated using an empirical relationship from Reymond et al. (2009):

$$D^i_{branch} = \rho^{-1} \cdot PWV^{i^{-2}} \tag{5}$$

where $PWV = 13.3d^{i^{-0.3}}$ and d^i is the branch diameter.

To calculate C^i_{WK3}, the arterial network was first lumped as a single-WK3 analogue (Figure 1d). This allowed us to determine the total arterial compliance, C_{tot}, using a method described by Les et al. (2010). Using $Q_{SI}(t)$ as an input to this lumped arterial network, WK3 parameters were adjusted until target values of P_{sa} and P_{da} were met. The peripheral compliance $C_{per} = C_{tot} - \Sigma C^i_V$ was divided between each outlet proportionally to their mean flow rates $\bar{Q}^i$:

$$C^i_{WK3} = \frac{\bar{Q}^i}{\bar{Q}_{SI}} \cdot C_{per} \tag{6}$$

The total resistance of each outlet was calculated using:

$$R^i_{tot} = R^i_p + R^i_d = \frac{\bar{P}}{\bar{Q}^i} \tag{7}$$

where $\bar{P} = 0.4P_{sa} + 0.6P_{da}$. An initial guess of R_p^i was obtained to match the characteristic impedance of the vessel:

$$R_p^i = \frac{\rho \cdot PWV^i}{A_{branch}^i} \tag{8}$$

where A_{branch}^i is the cross-sectional area of the branch outlet. Finally, each R_p^i was optimised so that the system achieved target values of P_{sa} and P_{da}. The final WK3 parameters are shown in Table 1.

[Table 1 about here.]

2.4. Wall Compliance

In our moving mesh approach (Bonfanti et al., 2017), the structural dynamics of the wall are not explicitly modelled. Instead, the magnitude of displacement of each mesh node at the aortic wall, δ_n, is computed as a linear function of the local pressure in the surface-normal direction $\mathbf{n}_n$:

$$\delta_n = \frac{p_n - p_{ext}}{K_n}\mathbf{n}_n \tag{9}$$

where K_n is the stiffness coefficient, p_n is the fluid pressure, and p_{ext} is the pressure exerted from the external side of the aortic wall, set to the diastolic pressure P_{da}. K_n is calculated (Figure 1f) using:

$$K_n = \frac{2}{C_A^i}\sqrt{\pi A_n} \tag{10}$$

where A_n is the cross-sectional area of the lumen at node n. $C_A^i = D^i \cdot A_{min}^i$ is the area compliance in the region of node n, where D^i values are obtained from equation 4.

We also performed a simulation with rigid walls to assess the impact of compliance on parameters of interest. In the rigid 0D model, the capacitors in each RLC unit representing the CFD domain were removed, and identical pressure and flow rate values were targeted. This resulted in a separate set of WK3 parameters for each simulation (Table 1).

2.5. CFD Simulation

The transient, three-dimensional Navier-Stokes equations were solved numerically using the finite-volume solver Ansys CFX 20.0 (Figure 1g). Blood was modelled as an incompressible non-Newtonian fluid using the Carreau-Yasuda viscosity model with empirical constants from Gijsen et al. (1999) and a density of 1056 kg/m^3. Using the Reynolds number (Re) definitions for pulsatile cardiovascular flow from Peacock et al. (1998), a nominal shear rate defined by Cagney and Balabani (2019), and the peak velocity from 4D-Flow MRI, the peak Re_p of 4157 was observed to exceed the critical Re_c of 3505, indicating the onset of turbulence. The k-ω Shear Stress Transport (SST) Reynolds-Averaged formulation of the Navier-Stokes equations was employed to model turbulence due to its ability to reasonably predict the onset and amount of flow separation under adverse pressure gradients (Lantz et al., 2011). A low turbulence intensity of 1% was applied at the inlet and outlets, which was found to most accurately represent healthy aortic flow by Kousera et al. (2013). Timesteps of 1 ms were solved using the implicit, second-order backward-Euler method. A root-mean-square residual value of 10^{-5} was achieved for all equations within each timestep. Simulations were run until periodic conditions were achieved, defined as less than 1% change in systolic and diastolic pressures between cycles, requiring five cycles in the compliant simulation and three in the rigid simulation.

3. Results

Inlet pressure and mean outlet flow rates were compared to target values to assess whether the WK3 BCs yielded physiological pressure and flow conditions. Targets for P_{sys}, P_{dia} and $\bar{Q}_i$ were achieved within 3.3% for both rigid and compliant simulations (Table 2).

[Table 2 about here.]

Volume flow rate from compliant and rigid simulations across the cardiac cycle were compared against 4D-Flow MRI measurements at DA1-DA4 (Figure 2). As mass conservation is not observed between the arch and abdominal aorta in 4D-Flow MRI but is enforced in the simulations, 4D-Flow MRI data measurements were scaled at each cross-section to match the stroke volume (SV) from simulations following the approach of Bäumler et al. (2020). Unscaled 4D-Flow MRI measurements are also shown as a band encapsulating ±22ml of stroke volume, representing the mean SV uncertainty for single-VENC 4D-Flow MRI data (Kroeger et al., 2021).

[Figure 2 about here.]

Simulated luminal cross-sectional area changes across the cardiac cycle were compared with 2D Cine-MR measurements at the arch and DA1-DA4 (Figure 3). Close agreement was observed throughout. Minor discrepancies in the shape of the area waveforms between CFD and MRI include a faster rate of area expansion during the acceleration phase in CFD, an earlier peak, and a more pronounced secondary peak at end-systole. Maximum and minimum areas matched closely at the arch, though with an in-plane resolution of only 4 mm x 1.25 mm, MRI measurements appear noisy and CFD and MRI waveforms do not appear as closely aligned.

[Figure 3 about here.]

Velocity magnitude contours from compliant and rigid CFD simulations were compared with 4D-Flow MRI data at peak systole (T1, Figure 4) and during mid-deceleration (T2, Figure 5), showing excellent agreement. It should be noted that CFD analysis planes were chosen to match the angle and location of 4D-Flow MRI planes and thus were not perpendicular to the centreline. At T1, a slight enlargement of the separation zone in the rigid simulation is observed across the aortic arch due to its smaller cross-sectional area. The peak velocity at T1 is better predicted by the compliant than the rigid simulation. Peak velocity is slightly under-predicted from DA2 to DA4 by both simulations, possibly due to the local effects of branching vessels that were not modelled. At T2, rigid and compliant simulations show similar distributions, though, in contrast to T1, slightly higher peak velocities are seen in the rigid simulation. High-velocity regions in both simulations are rotated by $\approx 90^\circ$ compared with 4D-Flow MRI.

[Figure 4 about here.]

[Figure 5 about here.]

Using the definitions from Gallo et al. (2012), Time Averaged Wall Shear Stress (TAWSS) and Oscillatory Shear Index (OSI) contours from the compliant simulation are shown alongside contours of difference between compliant and rigid simulations in Figure 6, with simulated velocity streamlines to assist in their interpretation.

[Figure 6 about here.]

High TAWSS values (above 5 Pa, according to Lantz et al. (2012); Peng et al. (2019)) are observed in the ascending aorta near the inlet, within LCC and LSA, and at their bifurcation, in agreement with other studies (Boccadifuoco et al., 2018; Lantz et al., 2011). These regions are exposed to high-velocity flow near the wall (Figure 6a). Regions of high OSI are observed in the descending aorta where disturbed flow develops during diastole, and the WSS vector becomes highly misaligned with its average (Figure 6d). OSI was low within the supra-aortic branches, though isolated regions of high OSI are seen at their bifurcations and in the ascending aorta. This has been attributed to low backflow in the branches and the pulsatile separation and recirculation at their bifurcations (Lantz et al., 2011). Although the distribution of TAWSS and OSI were qualitatively similar in both rigid and compliant simulations, the rigid case exhibited substantially higher TAWSS with a 13% higher mean, a 16.4% higher maximum, and a 19.3% higher minimum value than the compliant case. These differences are concentrated in the proximal aorta (Figure 6c). As WSS indices have been identified as markers for disease progression, this has implications for the prognostic value of rigid-wall simulations that will be further discussed in Section 4.

4. Discussion

We have presented a novel, efficient methodology to model patient-specific vessel compliance in CFD simulations using MRI data alone. Our MBM-based technique eliminates the need for explicit structural modelling and multiple simulations to tune structural properties, thus substantially reducing simulation timescales compared with FSI. Furthermore, because patient-specific wall compliance is tuned locally at each region, high accuracy is achieved in wall movement throughout the aorta compared with FSI, where structural properties are typically assumed to be uniform. By comparing equivalent compliant and rigid simulations of a healthy aorta, we have provided further evidence that rigid simulations may not accurately reproduce physiologically accurate velocity and WSS distributions when wall movement is significant.

Previous efforts to reconstruct the haemodynamics of a compliant healthy aorta from MRI data with FSI could not accurately characterise the movement of the aortic wall, underpredicting the extent of luminal area expansion despite multiple simulations with varying structural properties (Boccadifuoco et al., 2018). This effect may be of greater concern in simulations of pathological aortae, for example, in the case of TBAD. In a recent FSI study of TBAD, aortic compliance was captured accurately in some but not all regions due to the assumption of uniform E throughout the aorta (Bäumler et al., 2020). The image-based compliance tuning technique in the present study enabled patient-specific regional variations in compliance without the need for compliance tuning, resulting in excellent agreement with 2D Cine-MRI in luminal cross-sectional area change throughout the aorta.

Under the same pulse pressure, the compliant aorta produced a higher peak flow rate and a more negative flow rate at end-systole than the rigid simulation, resulting in favourable agreement with 4D-Flow MRI data in the compliant case. This effect is expected due to the accumulation and subsequent ejection of flow from each aortic segment as it expands and contracts under pressure. Although compliance acts to delay the peak flow rate, the compliant simulation predicted a slightly earlier peak in flow rate than 4D-Flow MRI, mirroring the faster increase and earlier peak observed in area waveforms. This may indicate an under-prediction in compliance of the aortic arch and supra-aortic branches due to longitudinal compliance of the proximal aorta that is not modelled. Indeed, Pagoulatou et al. (2021) observed under-predictions in proximal aortic distensibility of 20-62% when longitudinal compliance was neglected. There is also uncertainty in the 2D Cine-MRI data due to spatial and temporal resolution, so smaller features of the area waveform may not be represented accurately by the imaging data.

Close agreement was observed between simulations and 4D-Flow MRI velocity contours, both in flow structure and peak velocity. However, simulations resolved the boundary layer with high resolution while MRI could not. The boundary layer thickness of $\approx$ 1mm (see 4) is much smaller than the highest achievable resolution of 4D-Flow MRI in the large vessels, which typically exceeds $2mm$ (Fathi et al., 2020). As discussed, the compliant simulation achieved a higher peak flow rate. This resulted in better agreement with 4D-Flow MRI than the rigid simulation, outweighing the velocity-lowering effect of increased cross-sectional area. Peak velocities were slightly higher and closer to 4D-Flow MRI measurements in the rigid simulation at T2. Regions of high velocity in the compliant simulation were more dispersed at T2 than the rigid case, which lowered the peak velocity. Because area measurements agree particularly well between compliant CFD and MRI at T2 (≈6.5s), higher MRI velocities may result from the effects of un-modelled local branching vessels or bulk movement of the aorta away from its diastolic centreline. However, imaging errors in 4D-Flow MRI may also contribute.

Without accurate resolution of the boundary layer or the location of the wall in 4D-Flow MRI, WSS indices extracted from these images will incur substantial uncertainties (Miyazaki et al., 2017; Piatti et al., 2017; Zimmermann et al., 2018). Despite under-predicting peak velocity values, the mean TAWSS in the rigid simulation was 13% higher than the compliant simulation. This provides further evidence that under identical, patient-specific and physiological pressure and flow conditions, rigid simulations may substantially over-predict WSS if wall movement is significant. The influence of WSS on the onset and progression of a multitude of cardiovascular diseases has been widely demonstrated (Mazzi et al., 2020). For example, specific WSS distribution characteristics have been identified as markers of aneurysm development (Chung and Cebral, 2015), and regions of low WSS have been associated with numerous adverse effects, including endothelial dysfunction and the formation of atherosclerotic regions (Wee et al., 2018). Due to the strong prognostic value of WSS, our results highlight the importance of compliance modelling.

There are some limitations to the presented method. The MBM cannot handle large deformations due to an associated deterioration of mesh quality. Wall movement can be in the order of 10mm in pathologies such as TBAD

(Bäumler et al., 2020; Yang et al., 2014), so further work aims to improve the robustness of this technique to large deformations. Our methodology considers wall movement in the surface-normal direction, so any longitudinal compliance or bulk movement of the aorta is not modelled. Additionally, the effects of surrounding tissues are not considered, and the wall is assumed to exhibit linear elastic behaviour. These assumptions may contribute to differences in velocity contours between 4D-Flow MRI and CFD in the proximal aorta, where the movement of the aorta away from its diastolic centreline is most significant. These effects may also impact pressure wave transmission and contribute to the minor discrepancies in flow rate and luminal cross-sectional area curves between CFD and MRI. Despite numerous reports that the impact of the inlet velocity profile is negligible beyond the aortic arch, complex inlet flow may still have an impact further downstream and may contribute to discrepancies in velocity between CFD and 4D-Flow MRI throughout the aorta. We are currently extending this work to investigate the effects of inlet velocity conditions.

This study represents a significant methodological advance in its ability to accurately reconstruct patient-specific compliant aortic haemodynamics in a cost-efficient manner using MRI data alone. Our method exhibits numerous advantages over rigid-wall simulations and FSI simulations and could facilitate improved patient safety whilst minimising healthcare resources and reducing clinical decision-making timescales. Our technique could be generalised to other types of cardiovascular flows and to aortic diseases whose morphological features can be accurately captured with MRI.

Acknowledgements

This project was supported by the Wellcome/ EPSRC Centre for Interventional and Surgical Sciences (WEISS) (203145Z/16/Z), the British Heart Foundation (NH/20/1/34705), and the Department of Mechanical Engineering at University College London. The authors would also like to thank the Department of Computer Science of University College London for the high-performance computing cluster resources used to perform the simulations.

Conflict of Interest

The authors declare no conflicts of interest.

Appendices

Appendix A Prismatic Layers

In all meshes used for this study, ten prismatic layers with a first-layer thickness corresponding to a $y+$ of 1 were used to ensure that the first cell height lay within the viscous sublayer of the turbulent boundary layer. The total thickness of the prismatic layers exceeded the expected boundary layer thickness, δ, of 1.0 mm, estimated as $\delta = \sqrt{\nu/\Omega}$, where ν is the kinematic viscosity, and Ω is the cycle frequency (Pier and Schmid, 2017).

Appendix B Mesh Independence

Three successively refined meshes were used to perform a rigid-wall transient simulation with identical WK3 boundary conditions. Mesh element count approximately doubled between successive refinements, and the total prismatic layer thickness never fell below the expected boundary layer thickness of 1.0mm. Simulations were initialised using a previously converged simulation, and two further cycles were run. Less than 1% change in systolic and diastolic pressures were observed between these two cycles for each mesh. Key metrics from the final cycle of each of the three simulations are shown in Table 3.

[Table 3 about here.]

Percentage differences between coarse and medium meshes were an average of 3.4 times higher across all metrics than between medium and fine meshes. Differences between medium and fine meshes did not exceed 3.6% for all metrics, similar to acceptable differences noted in similar studies, so the medium mesh was used for all further analysis.

References

Armour, C.H., Guo, B., Pirola, S., Saitta, S., Liu, Y., Dong, Z., Xu, X.Y., 2020. The influence of inlet velocity profile on predicted flow in type B aortic dissection. Biomechanics and Modeling in Mechanobiology 20, 481–490.

Bäumler, K., Vedula, V., Sailer, A.M., Seo, J., Chiu, P., Mistelbauer, G., Chan, F.P., Fischbein, M.P., Marsden, A.L., Fleischmann, D., 2020. Fluid-structure interaction simulations of patient-specific aortic dissection. Biomechanics and Modeling in Mechanobiology 19, 1607–1628.

Boccadifuoco, A., Mariotti, A., Capellini, K., Celi, S., Salvetti, M.V., 2018. Validation of numerical simulations of thoracic aorta hemodynamics: Comparison with in vivo measurements and stochastic sensitivity analysis. Cardiovascular Engineering and Technology 9, 688–706.

Bonfanti, M., Balabani, S., Alimohammadi, M., Agu, O., Homer-Vanniasinkam, S., Díaz-Zuccarini, V., 2018. A simplified method to account for wall motion in patient-specific blood flow simulations of aortic dissection: Comparison with fluid-structure interaction. Medical Engineering & Physics 58, 72–79.

Bonfanti, M., Balabani, S., Greenwood, J.P., Puppala Sapna, Homer-Vanniasinkam Shervanthi, Díaz-Zuccarini Vanessa, 2017. Computational tools for clinical support: a multi-scale compliant model for haemodynamic simulations in an aortic dissection based on multi-modal imaging data. Journal of the Royal Society Interface 14.

Bozzi, S., Morbiducci, U., Gallo, D., Ponzini, R., Rizzo, G., Bignardi, C., Passoni, G., 2017. Uncertainty propagation of phase contrast-MRI derived inlet boundary conditions in computational hemodynamics models of thoracic aorta. Computer Methods in Biomechanics and Biomedical Engineering 20, 1104–1112.

Cagney, N., Balabani, S., 2019. Influence of shear-thinning rheology on the mixing dynamics in Taylor-Couette flow. Chemical Engineering and Technology 42, 1680–1690.

Castagna, M., Levilly, S., Paul-Gilloteaux, P., Moussaoui, S., Rousset, J.M., Bonnefoy, F., Idier, J., Serfaty, J.M., Le Touzé, D., 2021. An LDV based method to quantify the error of PC-MRI derived wall shear stress measurement. Scientific Reports 11, 4112.

Chung, B., Cebral, J.R., 2015. CFD for evaluation and treatment planning of aneurysms: review of proposed clinical uses and their challenges. Annals of Biomedical Engineering 43, 122–138.

Fathi, M.F., Perez-Raya, I., Baghaie, A., Berg, P., Janiga, G., Arzani, A., D'Souza, R.M., 2020. Super-resolution and denoising of 4d-flow mri using physics-informed deep neural nets. Computer Methods and Programs in Biomedicine 197, 105729.

Gallo, D., De Santis, G., Negri, F., Tresoldi, D., Ponzini, R., Massai, D., Deriu, M.A., Segers, P., Verhegghe, B., Rizzo, G., Morbiducci, U., 2012. On the use of in vivo measured flow rates as boundary conditions for Image-Based hemodynamic models of the human aorta: Implications for indicators of abnormal flow. Annals of Biomedical Engineering 40, 729–741.

Gijsen, F.J.H., van de Fosse, F.N., Janssen, J.D., 1999. The influence of the non-Newtonian properties of blood on the flow in large arteries: steady F flow in a carotid bifurcation model . Journal of Biomechanics 32, 601–608.

Goubergrits, L., Mevert, R., Yevtushenko, P., Schaller, J., Kertzscher, U., Meier, S., Schubert, S., Riesenkampff, E., Kuehne, T., 2013. The impact of MRI-based inflow for the hemodynamic evaluation of aortic coarctation. Annals of Biomedical Engineering 41, 2575–2587.

He, F., Hua, L., Guo, T., 2021. Numerical modeling in arterial hemodynamics incorporating fluid-structure interaction and microcirculation. Theoretical Biology and Medical Modelling 18, 6.

Henningsson, M., Malik, S., Botnar, R., Castellanos, D., Hussain, T., Leiner, T., 2020. Black-blood contrast in cardiovascular mri. Journal of Magnetic Resonance Imaging , e27399.

Kousera, C.A., Wood, N.B., Seed, W.A., Torii, R., O'Regan, D., Xu, X.Y., 2013. A numerical study of aortic flow stability and comparison with in vivo flow measurements. Journal of Biomechanical Engineering 135, 011003.

Kroeger, J.R., Pavesio, F.C., Mörsdorf, R., Weiss, K., Bunck, A.C., Baeßler, B., Maintz, D., Giese, D., 2021. Velocity quantification in 44 healthy volunteers using accelerated multi-VENC 4D flow CMR. European Journal of Radiology 137, 109570.

Lantz, J., Gårdhagen, R., Karlsson, M., 2012. Quantifying turbulent wall shear stress in a subject specific human aorta using large eddy simulation. Medical Engineering & Physics 34, 1139–1148.

Lantz, J., Renner, J., Karlsson, M., 2011. Wall shear stress in a subject specific human aorta – influence of fluid-structure interaction. International Journal of Applied Mechanics 03, 759–778.

Les, A.S., Shadden, S.C., Figueroa, C.A., Park, J.M., Tedesco, M.M., Herfkens, R.J., Dalman, R.L., Taylor, C.A., 2010. Quantification of hemodynamics in abdominal aortic aneurysms during rest and exercise using magnetic resonance imaging and computational fluid dynamics. Annals of Biomedical Engineering 38, 1288–1313.

Madhavan, S., Kemmerling, E.M.C., 2018. The effect of inlet and outlet boundary conditions in image-based CFD modeling of aortic flow. BioMedical Engineering OnLine 17, 66.

Mazzi, V., Gallo, D., Calò, K., Najafi, M., Khan, M.O., De Nisco, G., Steinman, D.A., Morbiducci, U., 2020. A eulerian method to analyze wall shear stress fixed points and manifolds in cardiovascular flows. Biomechanics and Modeling in Mechanobiology 19, 1403–1423.

McElroy, M., Keshmiri, A., 2018. Impact of using conventional Inlet/Outlet boundary conditions on haemodynamic metrics in a Subject-Specific rabbit aorta. Proceedings of the Institution of Mechanical Engineers, Part H 232, 103–113.

Miyazaki, S., Itatani, K., Furusawa, T., Nishino, T., Sugiyama, M., Takehara, Y., Yasukochi, S., 2017. Validation of numerical simulation methods in aortic arch using 4D flow MRI. Heart Vessels 32, 1032–1044.

Pagoulatou, S.Z., Ferraro, M., Trachet, B., Bikia, V., Rovas, G., Crowe, L.A., Vallée, J.P., Adamopoulos, D., Stergiopulos, N., 2021. The effect of the elongation of the proximal aorta on the estimation of the aortic wall distensibility. Biomechanics and Modeling in Mechanobiology 20, 107–119.

Peacock, J., Jones, T., Tock, C., Lutz, R., 1998. The onset of turbulence in physiological pulsatile flow in a straight tube. Experiments in Fluids 24, 1–9.

Peng, L., Qiu, Y., Yang, Z., Yuan, D., Dai, C., Li, D., Jiang, Y., Zheng, T., 2019. Patient-specific computational hemodynamic analysis for interrupted aortic arch in an adult: Implications for aortic dissection initiation. Scientific Reports 9, 8600.

Piatti, F., Pirola, S., Bissell, M., Nesteruk, I., Sturla, F., Della Corte, A., Redaelli, A., Votta, E., 2017. Towards the improved quantification of in vivo abnormal wall shear stresses in BAV-affected patients from 4d-flow imaging: Benchmarking and application to real data. Journal of Biomechanics 50, 93–101.

Pier, B., Schmid, P., 2017. Linear and nonlinear dynamics of pulsatile channel flow. Journal of Fluid Mechanics 815, 435–480.

Pirola, S., Jarral, O.A., O'Regan, D.P., Asimakopoulos, G., Anderson, J.R., Pepper, J.R., Athanasiou, T., Xu, X.Y., 2018. Computational study of aortic hemodynamics for patients with an abnormal aortic valve: The importance of secondary flow at the ascending aorta inlet. APL Bioengineering 2, 026101.

Pons, R., Guala, A., Rodríguez-Palomares, J.F., Cajas, J.C., Dux-Santoy, L., Teixidó-Tura, G., Molins, J.J., Vázquez, M., Evangelista, A., Martorell, J., 2020. Fluid-structure interaction simulations outperform computational fluid dynamics in the description of thoracic aorta haemodynamics and in the differentiation of progressive dilation in marfan syndrome patients. Royal Society Open Science 7, 191752.

Qiao, Y., Zeng, Y., Ding, Y., Fan, J., Luo, K., Zhu, T., 2019. Numerical simulation of two-phase non-newtonian blood flow with fluid-structure interaction in aortic dissection. Computer Methods in Biomechanics and Biomedical Engineering 22, 620–630.

Reymond, P., Merenda, F., Perren, F., Rüfenacht, D., Stergiopulos, N., 2009. Validation of a one-dimensional model of the systemic arterial tree. American Journal of Physiology-Heart and Circulatory Physiology 297, 208–222.

Ryzhakov, P., Soudah, E., Dialami, N., 2019. Computational modeling of the fluid flow and the flexible intimal flap in type b aortic dissection via a monolithic arbitrary lagrangian/eulerian fluid-structure interaction model. International Journal for Numerical Methods in Biomedical Engineering 35, e3239.

Saitta, S., Pirola, S., Piatti, F., Votta, E., Lucherini, F., Pluchinotta, F., Carminati, M., Lombardi, M., Geppert, C., Cuomo, F., Figueroa, C.A., Xu, X.Y., Redaelli, A., 2019. Evaluation of 4D flow MRI-based non-invasive pressure assessment in aortic coarctations. Journal of Biomechanics 94, 13–21.

Tang, E., Wei, Z.A., Fogel, M.A., Veneziani, A., Yoganathan, A.P., 2020. Fluid-structure interaction simulation of an intra-atrial fontan connection. Biology 9.

Wee, I., Ong, C.W., Syn, N., Choong, A., 2018. Computational fluid dynamics and aortic dissections: Panacea or panic? Vascular and Endovascular Review 1, 27–29.

Westerhof, N., Stergiopoulos, N., Noble, M., 2010. Snapshots of Hemodynamics: An Aid for Clinical Research and Graduate Education. 2 ed., Springer US, New York, New York. pp. 191,246.

Yang, S., Li, X., Chao, B., Wu, L., Cheng, Z., Duan, Y., Wu, D., Zhan, Y., Chen, J., Liu, B., Ji, X., Nie, P., Wang, X., 2014. Abdominal aortic intimal flap motion characterization in acute aortic dissection: assessed with retrospective ECG-gated thoracoabdominal aorta dual-source CT angiography. PLoS One 9.

Youssefi, P., Gomez, A., Arthurs, C., Sharma, R., Jahangiri, M., Alberto Figueroa, C., 2017. Impact of Patient-Specific Inflow Velocity Profile on Hemodynamics of the Thoracic Aorta. Journal of Biomechanical Engineering 140.

Zimmermann, J., Demedts, D., Mirzaee, H., Ewert, P., Stern, H., Meierhofer, C., Menze, B., Hennemuth, A., 2018. Wall shear stress estimation in the aorta: Impact of wall motion, spatiotemporal resolution, and phase noise. Journal of Magnetic Resonance Imaging 48, 718–728.

List of Figures

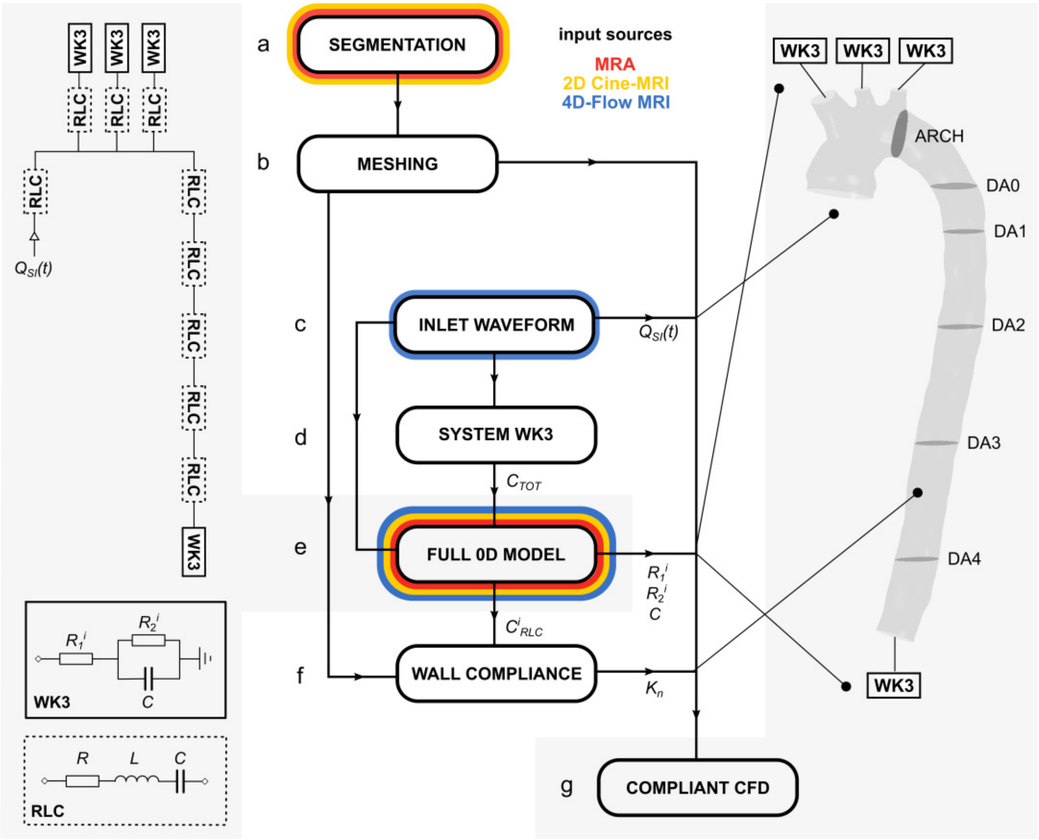

Figure 1: *Flowchart of the simulation methodology including schematic diagrams of the 0D domain (e) and the 3D CFD domain (g). Steps (a) through (g) are referred to throughout Section 2, where they are each described in detail.*

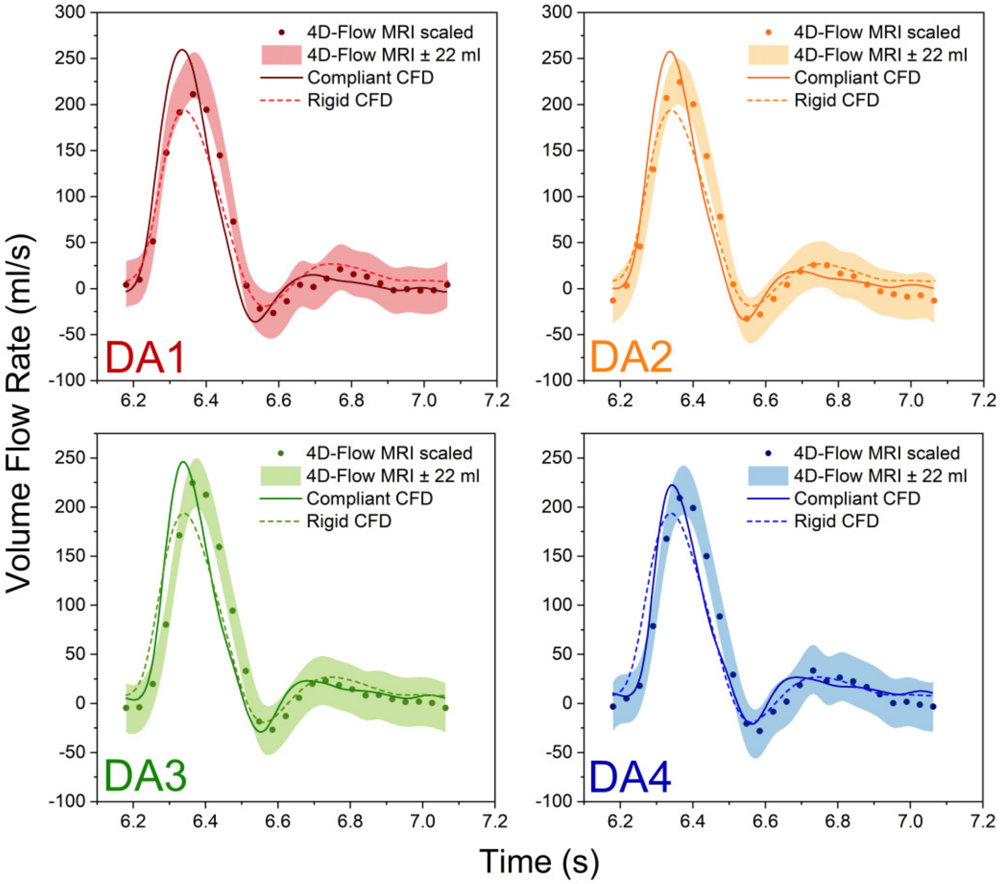

Figure 2: *Volume flow rate comparison between compliant and rigid CFD and 4D-Flow MRI at four planes in the descending aorta (see Figure 4 for locations). 4D-Flow MRI results are shown as a band with a 22 ml uncertainty in stroke volume, found to be the mean uncertainty for single-VENC 4D-Flow MRI measurements of flow rate by Kroeger et al. (2021). 4D-Flow MRI results are also shown as discrete measurements, with the stroke volume scaled to match CFD due to the lack of 4D-Flow MRI mass conservation.*

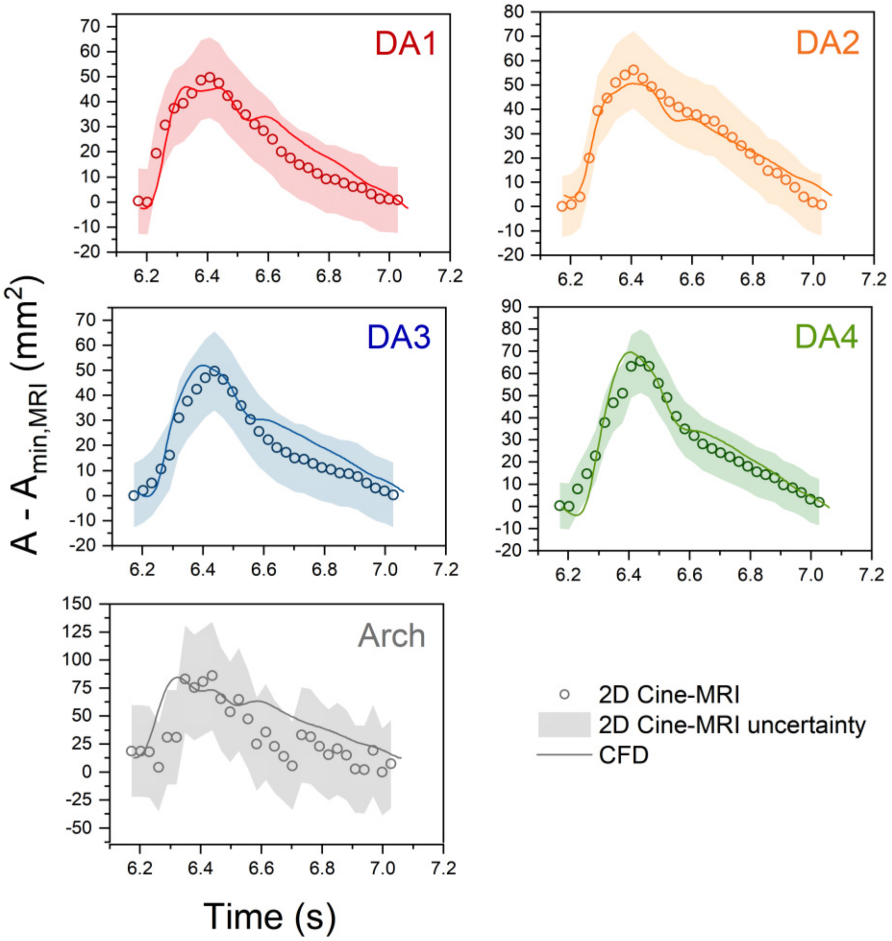

Figure 3: *Absolute luminal cross-sectional area comparison between 2D Cine-MRI and compliant CFD at the arch and descending aorta across the cardiac cycle. A band encapsulating ±6% error are indicated in the DA planes and ±12% at the arch. These errors were calculated by manually selecting the smallest and largest areas that could reasonably be chosen at each plane in GTFlow. See Figure 4 for plane locations.*

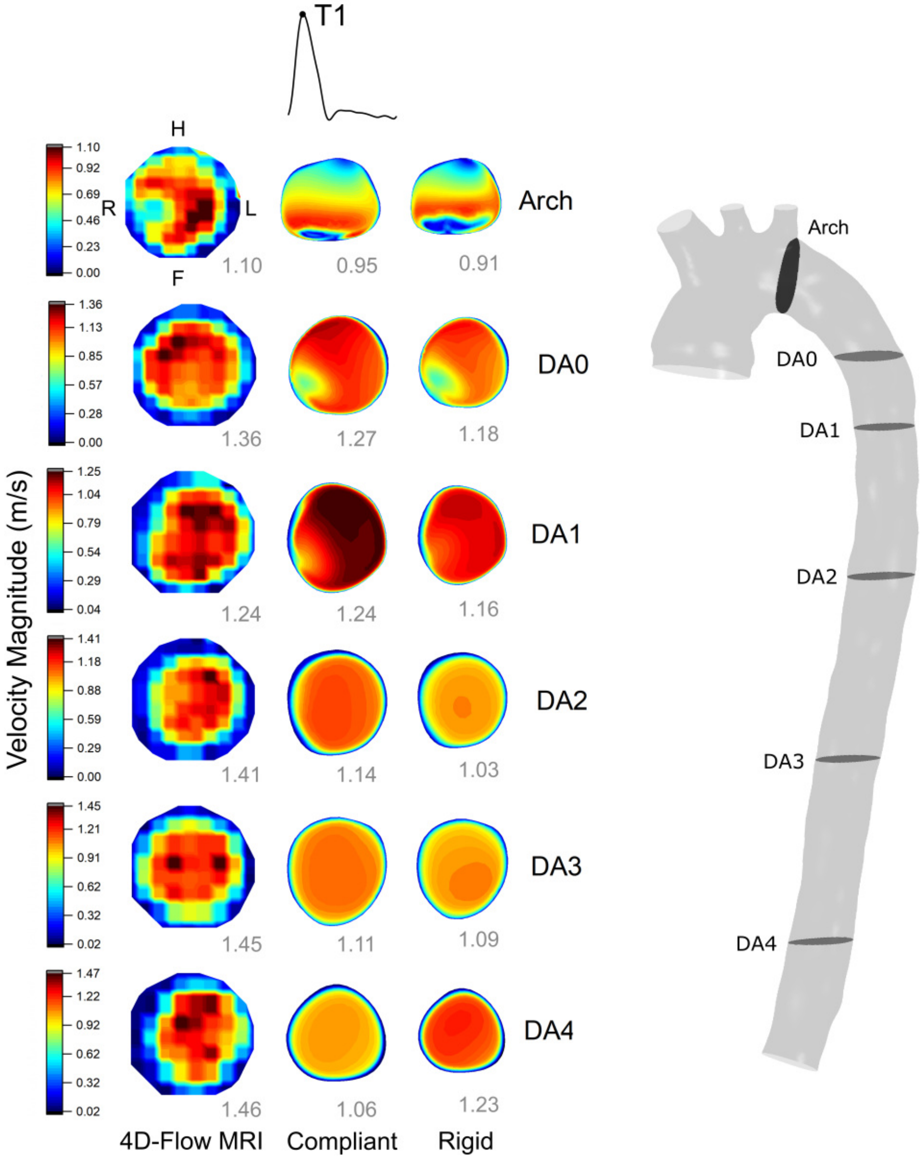

Figure 4: *Velocity contour comparison between 4D-Flow MRI, compliant and rigid CFD simulations at peak systole throughout the aorta. Velocity contour ranges are set by the minimum and maximum values from 4D Flow-MRI, and the peak velocity magnitude at each CFD plane is indicated at the bottom right of each contour. The arch plane orientation is indicated, while the orientation of the DA planes are indicated in Figure 5*

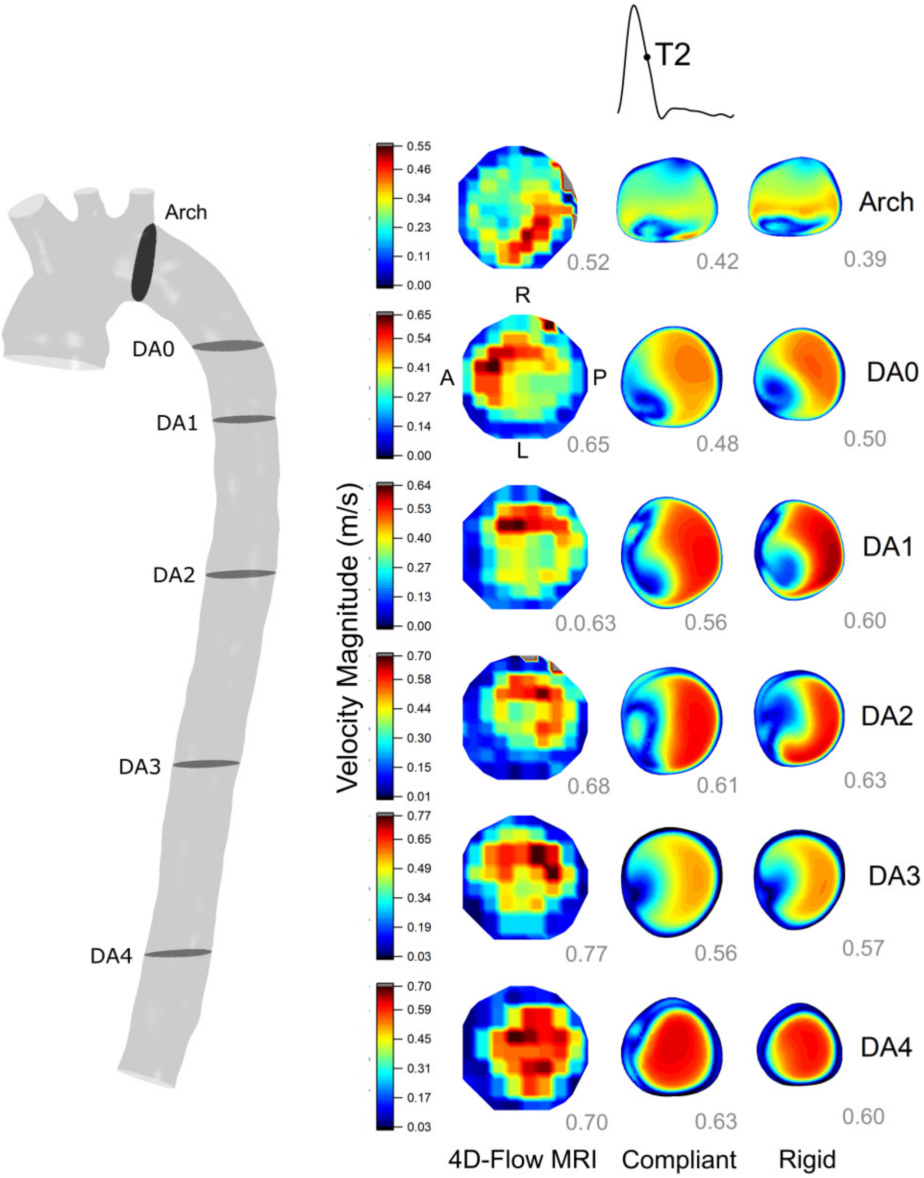

Figure 5: *Velocity contour comparison between 4D-Flow MRI, compliant and rigid CFD simulations at mid-deceleration throughout the aorta. Velocity contour ranges are set by the minimum and maximum values from 4D Flow-MRI, and the peak velocity magnitude at each CFD plane are indicated at the bottom right of each contour. The DA plane orientation is indicated, while the orientation of the arch planes are indicated on Figure 4*

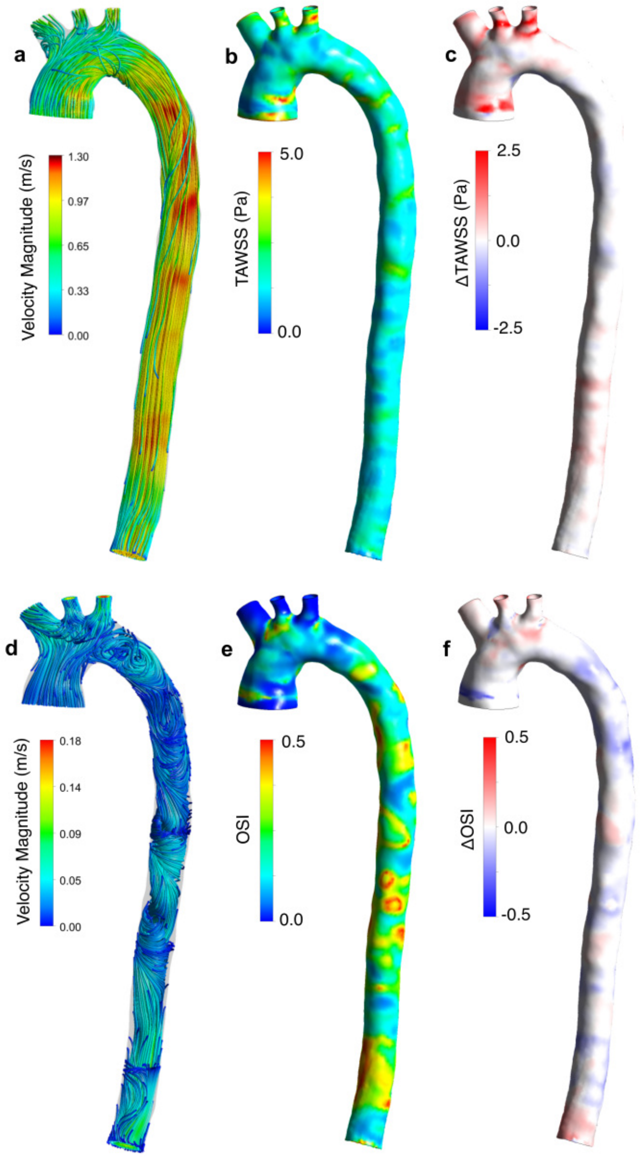

Figure 6: *a) Velocity streamlines at peak systole, b) TAWSS contours from the compliant simulation, clipped at 5 Pa, c) contours of TAWSS difference between compliant and rigid simulations, d) velocity streamlines during diastole, e) OSI contours from the compliant simulation f) contours of OSI difference between compliant and rigid simulations.*

List of Tables

Table 1: *Patient-specific three-element Windkessel parameters for compliant and rigid CFD simulations, determined using the 0D tuning process described in Section 2*

		BT	**LCC**	**LSA**	**AbAo**
Compliant	R_1 $(mmHg/ml/s)$	0.4872	0.9744	0.9179	0.1154
	R_2 $(mmHg/ml/s)$	4.2231	9.7188	6.3783	1.8281
	C $(ml/mmHg)$	0.3818	0.1682	0.2465	0.5702
Rigid	R_1 $(mmHg/ml/s)$	0.1500	0.2500	0.2500	0.0750
	R_2 $(mmHg/ml/s)$	4.5600	10.4430	7.0460	1.8690
	C $(ml/mmHg)$	0.3818	0.1682	0.2465	0.5702

Table 2: *Simulated compliant and rigid inlet systolic and diastolic pressure and mean outlet flow rates compared with target values. The percentage error between simulated and target values are indicated.*

Quantity	**Measurement**	**Target**	**Rigid / % err**	**Compliant / % err**
P_{sys} (mmHg)	117	108	104.9 / 2.9%	105.1 / 2.7%
P_{dia} (mmHg)	72	72	69.6 / 3.3%	71.7 / 0.4%
$\bar{Q}_{BT}$ (ml/s)	13.57	18.34	18.20 / 0.8%	17.99 / 1.9%
$\bar{Q}_{LCC}$ (ml/s)	6.17	8.11	8.02 / 1.1%	7.99 / 1.5%
$\bar{Q}_{LSA}$ (ml/s)	4.37	11.84	11.52 / 2.7%	11.51 / 2.8%
$\bar{Q}_{AbAo}$ (ml/s)	44.60	44.44	44.20 / 0.4%	44.73 / 0.9%

Table 3: *Table of key metrics from coarse, medium and fine (C, M, F) rigid-wall simulations. Final two columns show the percentage difference between medium/coarse and fine/medium meshes. T1 refers to peak systole. Velocity metrics are calculated across all cells in the domain, while pressure metrics are measured only at the wall surface.*

	Coarse	**Medium**	**Fine**	**% diff: M/C**	**% diff: F/M**
Node count	68465	186202	418977	63.2	55.6
Element count	199076	525274	1199742	62.1	56.2
Avg. pressure @ T1: wall	96.02	95.78	95.67	-0.25	-0.11
Max. pressure @ T1: wall	111.35	111.63	111.70	0.25	0.06
Avg. vel. mag @ T1	0.67	0.64	0.62	-4.75	-3.56
Max. vel. mag. @ T1	1.85	1.85	1.87	0.018	0.81
Mean TAWSS	1.94	1.90	1.91	-2.18	0.40
Max. TAWSS	9.62	11.06	10.78	12.97	-2.66
Mean. OSI	0.151	0.153	0.153	1.71	-0.32